Extreme Mechanics Letters 74 (2025) 102271

Contents lists available at ScienceDirect

Extreme Mechanics Letters

journal homepage: www.elsevier.com/locate/eml

Simulating flow-induced reconfiguration by coupling corotational plate finite elements with a simplified pressure drag

Danick Lamoureux [a], Sophie Ramananarivo [b], David Melancon [a], Frédérick P. Gosselin [a,*]

[a] Laboratory for Multi-Scale Mechanics (LM2), Department of Mechanical Engineering, Polytechnique Montreal, 2500 chemin de Polytechnique, Montreal (Quebec), H3T1J6, Canada

[b] LadHyX, CNRS, École Polytechnique, Institut Polytechnique de Paris, 91120, Palaiseau, France

ARTICLE INFO

Keywords:
Fluid–structure interaction
Finite element analysis
Drag reduction by reconfiguration
Geometric nonlinearities
Wind on trees
Flow-induced deformation

ABSTRACT

Developing engineering systems that rely on flow-induced reconfiguration, the phenomenon where a structure deforms under flow to reduce its drag, requires design tools that can predict the behavior of these flexible structures. Current methods include using fully coupled computational fluid dynamics and finite element analysis solvers or highly specialized theories for specific geometries. Coupled numerical methods are computationally expensive to use and non-trivial to setup, while specialized theories are difficult to generalize and take a long time to develop. A compromise between speed, accuracy, and versatility is required to be implemented into the design cycle of flexible structures under flow. This paper offers a new numerical implementation of the pressure drag in the context of a corotational finite element formulation on MATLAB. The presented software is verified against different semi-analytical theories applied to slender plates and disks cut along their radii as well as validated against experiments on kirigami sheets and draping disks.

Usage: The developed code and verification cases presented here are available on GitHub https://github.com/lm2-poly/FIRM.

1. Introduction

Fluid flow can cause large deformations of flexible, natural structures such as trees [1], leaves [2–6], dandelions [7,8], wings [9], seaweeds [10], and other aquatic plants [11]. By deforming, these biological systems reduce their drag, thereby minimizing the reaction forces required to maintain integrity [6]. Inspired by this natural phenomenon called flow-induced reconfiguration [11,12], engineering applications have been proposed such as passive actuation of mechanical devices [13–15] and energy harvesting [16,17]. The development of these novel engineering systems rely on modeling the physics of flow-induced reconfiguration, which is currently numerically expensive or complex to develop.

Analytical and semi-analytical models have been developed to study the reconfiguration of slender structures, but they are specific to their corresponding systems, e.g., thin strips with [18] or without flaps [19], plates with [19,20] or without holes [4,21], disks with one cut [3], multiple cuts [4] or without cuts [22], kirigami sheets [14], and dandelions [7,8]. Computational fluid dynamics (CFD) software coupled with solid mechanics finite element analysis (FEA) software have been used to predict the reconfiguration of similar slender structures [23–26] and can be generalized to complex geometries. However, CFD-FEA coupled approaches are computationally expensive and complex to setup.

Hybrid solutions obtained by deriving an analytical solution for structural mechanics combined with CFD to define the fluid loading have been used [20], but also prove complex to setup. By taking inspiration from approaches similar to Taylor [27]'s semi-empirical drag model for rods set at an angle to incoming flow, analytical solutions have been derived by representing the effect of the fluid flow as a local pressure on the structure surface, which only depends on the local orientation of the structure with the flow [3,4,14]. These different models developed for reconfiguring rectangular plates [4], rolling disks [3], and deforming kirigami sheets [14] assume that pressure drag dominates over viscous skin friction as the Reynolds number range between 10,000 and 100,000. Bhati et al. [28] showed that the effect of skin friction on reconfiguration for Reynolds numbers larger than 1000 is minimal. The Reynolds number is defined here as the product of the free-stream flow velocity and the longest length of the bluff body divided by the kinematic viscosity of the fluid.

Here, we propose a finite element framework based on the corotational approach that uses the pressure field obtained from a uniform flow field on a structure to model flow-induced reconfiguration of

* Corresponding author.
E-mail address: frederick.gosselin@polymtl.ca (F.P. Gosselin).

https://doi.org/10.1016/j.eml.2024.102271
Received 6 June 2024; Received in revised form 11 September 2024; Accepted 24 November 2024
Available online 5 December 2024

flexible structures (see Fig. 1). This pressure field, which is formulated through a momentum conservation argument, has only been applied to simple geometries, typically using the Euler–Bernoulli beam equation. By implementing this fluid load within a finite element solver, we present a versatile framework, a general flow-induced reconfiguration model (FIRM), which we verify and validate on structures with increasing geometrical complexity. Our simulations successfully capture their highly nonlinear responses and match the trends predicted by semi-analytical models and experimental data reported in the literature. We conclude on a degenerate case that highlights the limitation of the FIRM framework.

2. Methodology

2.1. Pressure field formulation

When placed in a uniform flow, a thin structure, like a plate or a shell, creates a pressure difference on its windward and leeward sides, leading to pressure drag. To model this, we apply a similar modeling argument of momentum flux balance as Schouveiler and Boudaoud [3], but generalize it to more complex geometries. Assuming that the flow has reached a uniform permanent regime of flow velocity $\vec{U}$ (see Fig. 1a–b) and averaging out in time the dynamic phenomena such as vortex shedding or turbulence, the elemental force $\mathrm{d}\vec{F}$ produced in reaction to the flow can be derived from momentum conservation as

$$\mathrm{d}\vec{F} = \rho_f \vec{U} \left(\vec{U} \cdot \vec{n}\right) \mathrm{d}S, \tag{1}$$

where ρ_f is the fluid density. We define a Cartesian coordinate system xyz aligned with the flow such that $\vec{U} = U_\infty \vec{z}$. An infinitesimal planar element of area $\mathrm{d}S$ of the structure has its normal $\vec{n}$ and makes an angle θ with the flow. To obtain the resulting pressure p (see Fig. 1c), we project $\mathrm{d}\vec{F}$ along $\vec{n}$ and consider the force per unit area applied on this infinitesimal area

$$p(\theta) = \frac{1}{2}\rho_f U_\infty^2 C_D \cos^2\theta, \tag{2}$$

where C_D is the drag coefficient of the equivalent rigid structure so that the resulting drag of our reconfigurable structure can be compared to its rigid counterpart [4]. The drag coefficient C_D implicitly captures effects that are not otherwise modeled. For example, while the software does not explicitly depends on the Reynolds number, the drag coefficient C_D must be measured experimentally – or simulated with CFD – in the same conditions for the results to be applicable. Its value will be lightly affected by the Reynolds number. For simplicity, since we consider problems with Reynolds number values larger than 1000, we assume that pressure drag dominates over skin friction drag and thus neglect the latter [28].

To transform the drag back into the xyz reference frame, it is integrated it over the whole structure Ω such that

$$D = \int_\Omega \frac{1}{2}\rho_f U_\infty^2 C_D \cos^3\theta \mathrm{d}\Omega. \tag{3}$$

2.2. Corotational finite element framework

To simulate the deformation of the structure subjected to the pressure field $p(\theta)$ given by Eq. (2), we use an implementation of a corotational finite element model [29]. This method decouples the rigid body motions of elements from their local deformations therefore allowing large displacements and rotations, as expected in the context of reconfiguration [3,4,14]. The structure is first meshed with triangular elements using GMSH [30] (see Fig. 1d). Once meshed, the angle θ between the flow and the deformed structure is computed at each node by fitting a plane through its nearest neighboring nodes (see Fig. 1e and [31] for more details). The deformation-dependent pressure is applied to each node and the displacements u, v, w and rotations ϕ_x, ϕ_y, and ϕ_z are solved iteratively based on a finite element formulation that couples the Discrete Kirchhoff Triangle (DKT) plate theory to capture bending stresses of thin plates [32,33] and the Assumed Natural Deviatoric Strain (OPT) membrane theory to capture membrane stresses [34] (see Fig. 1f). Note that the material constitutive law is modeled as isotropic Hookean. We verify and validate the developed software using benchmark test cases (see [31] for more details). The finite element code is implemented in MATLAB and is available on GitHub [35].

2.3. Dimensional analysis

In the following, we use two main dimensionless numbers to characterize the reconfiguration of flexible structures: the Cauchy and reconfiguration numbers. The Cauchy number C_Y is defined as the ratio of the fluid load over the elastic restoring forces

$$C_Y = \frac{\rho_f U_\infty^2 C_D L_c}{K}, \tag{4}$$

with L_c a characteristic length and K the structure's stiffness in the appropriate deformation mode. Low Cauchy numbers indicate either low flow velocities or stiff structures, whereas high Cauchy numbers indicate higher fluid loading.

The reconfiguration number $\mathcal{R}$ relates the drag D of a deformable structure with that of a rigid equivalent D_{rigid}

$$\mathcal{R} = \frac{D}{D_{rigid}} = \frac{\int_\Omega \mathrm{d}F}{\frac{1}{2}\rho_f U_\infty^2 C_D S} = \frac{\sum_{i=1}^{N_e} \frac{1}{2}\rho_f U_\infty^2 C_D \cos^3\theta_i S_i}{\frac{1}{2}\rho_f U_\infty^2 C_D S} = \frac{\sum_{i=1}^{N_e} S_i \cos^3\theta_i}{S}, \tag{5}$$

where $S = \sum_{i=1}^{N_e} S_i$ is the structure's area summed over all N_e elements. A reconfiguration number close to unity indicates a drag that is close to that of the rigid structure, while a lower reconfiguration number reveals that the structure has deformed sufficiently to reduce its generated drag. Fig. 1g shows a typical $\mathcal{R}$-C_Y curve for a structure undergoing flow-induced reconfiguration. We see that at low Cauchy number, the reconfiguration number is close to unity in the rigid regime. As the Cauchy number is increased, a transition region first appears, followed by an asymptotic regime governed by $\mathcal{R} \sim C_Y^{\mathcal{V}/2}$, where $\mathcal{V}$ is Vogel's exponent [6]. Vogel's exponent is a term that describes the asymptotic drag reduction of a reconfigured structure, such that $D \sim U_\infty^{2+\mathcal{V}}$, and is typically negative [5,12].

3. Results

3.1. Flat rectangular plate

We first apply our Flow-Induced Reconfiguration Model (FIRM) to study the reconfiguration of a thin rectangular plate of width $W = 35\,\mathrm{mm}$, length $L = 50\,\mathrm{mm}$, and thickness $T = 0.1\,\mathrm{mm}$, clamped at one end and subjected to a flow of velocity U_∞ as schematized in the inset of Fig. 2a. We model the plate material with a Young's modulus of $E = 68\,\mathrm{GPa}$ and Poisson's ratio of $\nu = 0$, to approach a 1D beam behavior. We consider a rigid drag coefficient $C_D = 2.0$ and a fluid density $\rho_f = 1.225\,\mathrm{kg\,m^{-3}}$. The drag coefficient in itself will not matter due to the dimensionless numbers used, but we keep a drag coefficient similar to what is found by Gosselin et al. [4]. For this case, the Cauchy number is obtained from Eq. (4) with the characteristic length $L_c = L$ and the stiffness $K = 2B/L^2$ with $B = ET^3/12$ the bending stiffness. This leads to $C_Y = \rho_f U_\infty^2 C_D L^3/(2B)$. In order to improve solver efficiency, as the velocity is incremented, the previous solution serves as an initial guess for the next velocity iteration in a form of continuation method.

We show in Fig. 2a the $\mathcal{R}$-C_Y curve obtained via FIRM (solid blue line) and compare it against the results from a semi-analytical model (dashed line) based on Euler–Bernoulli beam theory that uses the same pressure formulation as in Eq. (2) [4]. We find excellent agreement between the two in each of the three regimes: (i) at low Cauchy number, i.e., $C_Y < 1$, the drag of the plate is similar to its rigid

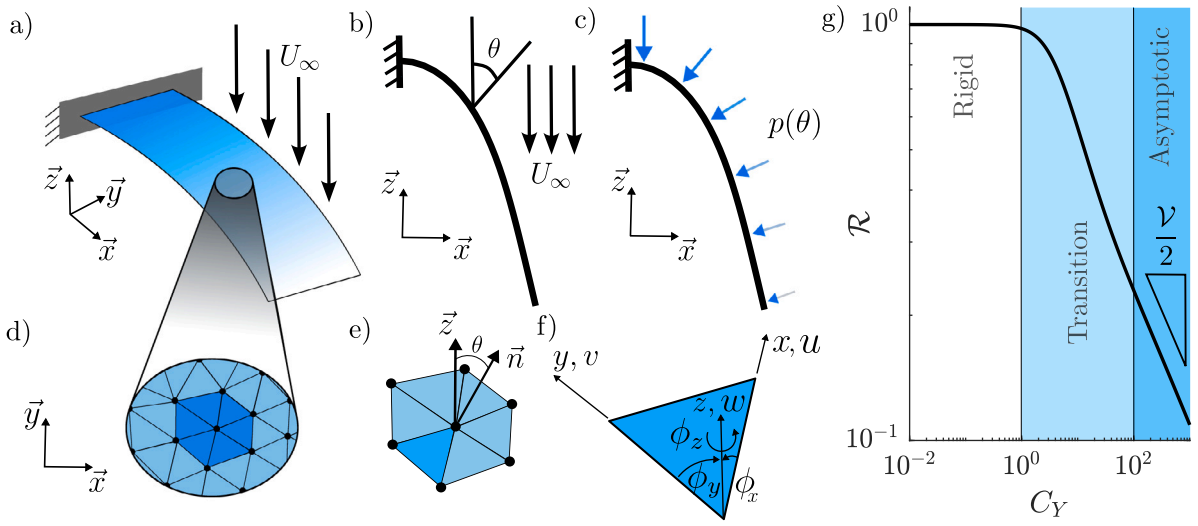

Fig. 1. Flow-Induced Reconfiguration Model (FIRM). (a) Schematic of a flexible structure reconfiguring under a flow of velocity U_∞. (b) The uniform flow field hits the structure at an angle θ that varies across the surface of the structure. (c) The flow-field is converted into a pressure field p that varies as a function of the local angle θ. The size of the arrows indicate the magnitude of the pressure as an example. (d) To compute its elastic deformation under flow, the structure is discretized using 2D triangular finite elements using GMSH. (e) The normal of each node $\vec{n}$ and the angle θ are calculated by fitting a plane through the nearest neighboring nodes. (f) The elements' formulation is based on a coupled Discrete Kirchhoff Triangle plate theory and the Assumed Natural Deviatoric Strain membrane theory with u, v, w, ϕ_x, ϕ_y, and ϕ_z the displacements and rotations along the x, y, and z axes. (f) Typical Reconfiguration number — Cauchy number curve, showing the three regimes (i) rigid behavior, (ii) transition region and (iii) Asymptotic behavior governed by the Vogel exponent. (For interpretation of the references to color in this figure legend, the reader is referred to the web version of this article.)

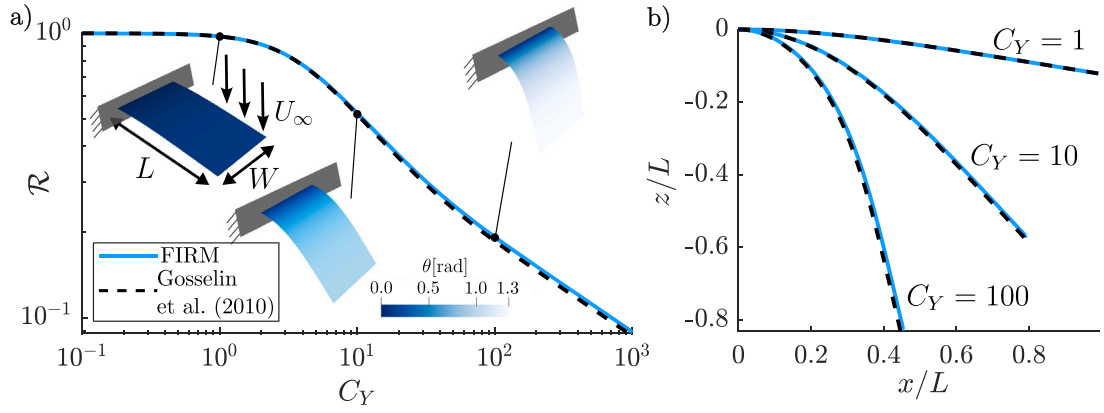

Fig. 2. Reconfiguration of a slender plate. (a) Reconfiguration number $\mathcal{R}$ as a function of the Cauchy number C_Y for a flat, slender plate of length L and width W. The color gradient on the plate illustrates the variation of the angle of the surface's normal with the flow as shown in the colorscale. (b) 2D deformed shapes of the flat rectangular plate under reconfiguration using normalized coordinates at $C_Y = \{1, 10, 100\}$. The dashed and solid lines represent the results from the semi-analytical model developed by Gosselin et al. (2010) and our FIRM model, respectively, as shown in (a)'s legend. (For interpretation of the references to color in this figure legend, the reader is referred to the web version of this article.)

counterpart ($\mathcal{R} \approx 1$), (ii) at intermediate Cauchy number, i.e., $C_Y \in [1, 100]$, there is a transition zone, and (iii) at high Cauchy number, i.e., $C_Y > 100$, $\mathcal{R}$ converges to an asymptotic behavior that can be described in terms of a Vogel exponent $\mathcal{V} = -2/3$. We show in the insets of Fig. 2a the deformation predicted by FIRM at $C_Y = \{1, 10, 100\}$ where the color gradient illustrates the angle the surface makes with the flow. These insets confirm that the deformation is strictly 2D. For the same Cauchy numbers, we plot in Fig. 2b the deformed 2D shapes of the plates in normalized coordinates $(x/L, z/L)$ and compare the results with the semi-analytical predictions [4]. Once again, we find excellent agreement for the three deformations we observe. These comparisons provide a verification of FIRM and an indirect validation, as Gosselin et al. [4] confronted their model to wind tunnel experiments and the soap film experiments of Alben et al. [2,36].

3.2. Circular plate with radial slits

Next, we simulate with FIRM a disk with radial slits held at its center which deforms in 3D under a flow of velocity U_∞ perpendicular to its undeformed shape. The disk has an external radius $R_e = 3.7\,\text{mm}$, inner uncut radius $R_i = 0.9\,\text{mm}$ and thickness $T = 0.1\,\text{mm}$ cut into $N = 36$ sectors, with its material modeled with a Young's modulus $E = 4.848\,\text{GPa}$ and Poisson's ratio $\nu = 0$. We consider a rigid drag coefficient $C_D = 2.0$ and a flow density $\rho_f = 1.225\,\text{kg m}^{-3}$. For this case, the Cauchy number is obtained from Eq. (4) with $L_c = R_e - R_i$ and $K = ET^3/\left(6\beta(R_e - R_i)^2\right)$, where $\beta = R_e/R_i$ the disk's taper ratio [4].

In Fig. 3a, we plot the $\mathcal{R}$-C_Y curve for the described disk obtained with the FIRM software (solid green line) and compare it with the previously discussed large deformation Euler–Bernoulli beam model of Gosselin et al. [4] (dashed line). It is a semi-analytical model, such that the model's formulation is analytical, but it requires numerical

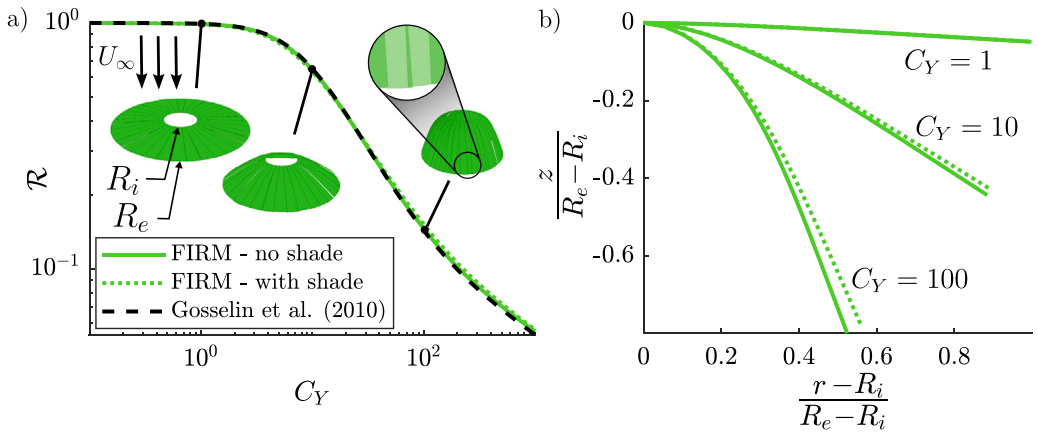

Fig. 3. Reconfiguration of a disk with radial slits. (a) Reconfiguration number $\mathcal{R}$ as a function of the Cauchy number C_Y of a disk of external radius R_e, clamped radius R_i with N slits using FIRM, with and without shading, compared to Gosselin et al. [4]'s model. The deformed structure is illustrated in the insets at Cauchy numbers of 1, 10 and 100, with the dimensions of the disk illustrated in the first inset. The last inset's zoom shows two blades covering each other, causing shading. The current curve is produced using a taper ratio $\beta = R_e/R_i = 4.111$ with $N = 36$ slits. (b) 2D deformed shape of a blade under shading and no shading in normalized coordinates at $C_Y = \{1, 10, 100\}$ as predicted by FIRM. (For interpretation of the references to color in this figure legend, the reader is referred to the web version of this article.)

resolution. There is again excellent agreement between the two models in the three previously identified regimes such that (i) for $C_Y < 1$, $\mathcal{R} \approx 1$, (ii) for $C_Y \in [1, 100]$, there is a transition region and (iii) for $C_Y > 100$, we reach an asymptotic regime that is described using a Vogel's exponent of $\mathcal{V} = -1$. The insets of Fig. 3a show the deformed shapes of the disk during these three different regimes. We note that as the blades bend under flow, they partially cover one another. This leads to shading, i.e., covered sections do not perceive the flow, and blade contact adds stiffness to the structure. In FIRM, we do not model contact and implement a simple shading law based on the exposed area of the structure (see [31] for more details about the implementation). We add to Fig. 3a the $\mathcal{R}$-C_Y curve for this disk using the modified FIRM with the simple shading law and plot in Fig. 3b, the deformed shape of a blade at $C_Y = \{1, 10, 100\}$ with (solid green line) and without (broken green line) shading using its normalized radial $(r - R_i)/(R_e - R_i)$ and vertical $z/(R_e - R_i)$ position. We find that shading has minor effect on the reconfiguration of the disk with radial slits.

3.3. Ribbon kirigami under flow

To demonstrate that FIRM is able to capture complex nonlinear behaviors such as buckling, we use it to simulate the reconfiguration of a ribbon kirigami sheet under flow clamped at both ends as shown in Fig. 4. We consider a sheet similar to that of Marzin et al. [14] with length $L = 121.6\,\text{mm}$, width $W = 108\,\text{mm}$, and thickness $T = 0.1\,\text{mm}$. The sheet is cut with $N_x = 5$ slits along its width and $N_y = 31$ slits along its length, as illustrated in the insets of Fig. 4a. We use a notation that is different than Marzin et al. [14] due to the modeling choices used during the simulation. However, we adapt the used parameters to obtain the same geometry. Slits are cut with length $L_s = 17.2\,\text{mm}$ and pitch spaced from one another by $2d_x$ along the width of the sheet, with $d_x = 2.2\,\text{mm}$, and $d_y = 3.8\,\text{mm}$ along the length of the sheet. The material is defined using a Young's modulus of $E = 4\,\text{GPa}$ and a Poisson's ratio of $\nu = 0.3$. The flowing fluid has a density $\rho_f = 997\,\text{kg}\,\text{m}^{-3}$. Finally, we consider a rigid structure drag coefficient $C_D = 2.0$.

For this case, the Cauchy number is obtained from Eq. (4) with $L_c = W$, and K the stretching stiffness of the sheet during its second linear regime once the sheet has buckled out of plane. Experimentally, when the sheet is clamped at both ends and stretched in-plane, a first regime is encountered, where the sheet observes in-plane strains, until a critical load where each beam buckle out of the plane, leading to a second, linear regime [14,37,38]. This second regime stretching stiffness, which is in $\text{N}\,\text{m}^{-1}$, is evaluated numerically through a tensile simulation as $K = 35.4\,\text{N}\,\text{m}^{-1}$ which is in good agreement with the reported value by Marzin et al. [14] of $K = 38.9\,\text{N}\,\text{m}^{-1}$ (see [31] for more details regarding the tensile simulation).

Importantly, the experiments of Marzin et al. [14] were conducted in a water channel of cross section $150\,\text{mm} \times 150\,\text{mm}$ with an area $S_{ch} = 22\,500\,\text{mm}^2$, of which the undeformed sheet occupies $S_0 = LW = 13\,133\,\text{mm}^2$. The undeformed sheet blocks 58.4% of the channel cross-section, which significantly confines the flow. As the sheet deforms under flow, its projected area is modified, changing the blockage ratio. To roughly estimate this effect, we use the same conservation of mass argument as Marzin et al. [14] and define the effective flow velocity

$$U^* = \frac{S_{ch}}{S_{ch} - S} U_\infty, \tag{6}$$

requiring the computation of the sheet frontal area S at each velocity increment.

Fig. 4 presents the simulation of the kirigami ribbon subjected to transverse flow. At small Cauchy, the sheet deforms purely as a membrane, then its beams or blades of material between the slits buckle out of plane, giving rise to bending deformation and nonlinear deformation with varying effective rigidity. In Fig. 4a, we show the normalized out-of-plane displacement z/L as a function of the Cauchy number C_Y obtained via FIRM (solid yellow line) with no blockage effects ($U^* = U_\infty$) and compare it with the experimental data from Marzin et al. [14]. Experimentally, the out-of-plane deformations of 19 different kirigami sheets collapse onto a master curve that increases monotonically according to the Cauchy number. The different kirigami sheets are identified through markers indicating series (circles are specimens with varied L_s, triangles with varied d_y and squares with varied d_x) and colors indicating which pattern they are precisely (we adopt the same convention as Marzin et al. [14] once adapted to our notation). We notice that, for a fixed value of C_Y, the deformation predicted by FIRM underestimates the value of $-z/L$, which is expected as we completely neglect the increase in flow velocity due to blockage. If we consider the other extreme of maximum blockage, i.e., assuming the kigirami sheet obstructs the channel with its undeformed frontal area $S_0 = LW$ for any value of C_Y, we find a slight overestimation of $-z/L$ shown with the yellow dashed line in Fig. 4a. Together, the curves assuming zero and maximum blockage create an envelope that encompasses most experimental measurements. By considering a variable blockage with Eq. (6) at every iteration of C_Y, we find the yellow dotted line in Fig. 4a that lies in-between the two previous assumptions. Using this variable blockage approach, we find good agreement with the experimental data and observe the same regimes as in the experiments, i.e., (i) for $C_Y < 10^{-2}$, the displacement remains small and the kirigami sheet deforms through in-plane stretching and

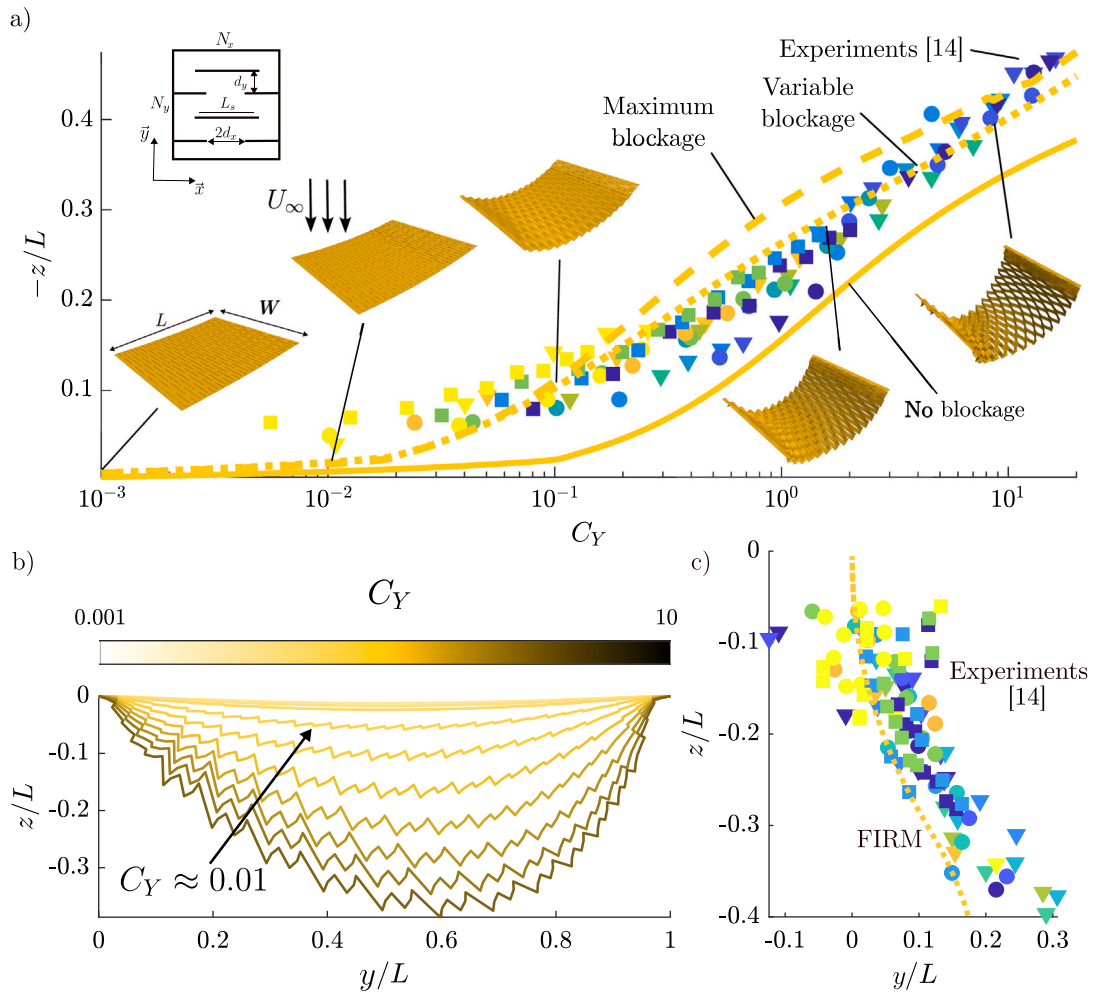

Fig. 4. Reconfiguration of a kirigami sheet under flow. (a) Dimensionless out-of-plane displacement z/L as a function of the Cauchy number C_Y of a flat kirigami sheet of length L, width W, and stiffness K using the current implementation (FIRM), with no blockage, maximum blockage, and variable blockage assumptions compared to Marzin et al. [14] experimental data. The markers and colors of the experimental data follow Marzin et al. [14]'s convention once adapted to our notation, where circles are a specimen series with varied L_s, triangles with varied d_y and squares with varied d_x. Insets show the sheet's deformed state at different Cauchy numbers, illustrating both in-plane stretching and post-buckling out-of-plane deformation. (b) Profile of the kirigami sheet's midplane at different Cauchy numbers in normalized deformed configuration using the variable blockage assumption. (c) Evolution of the asymmetric deformation of the sheet as the out-of-plane deformation increases using the variable area velocity formulation compared to Marzin et al. [14] experimental data. The markers and colors of the experimental data are the same as in (a). (For interpretation of the references to color in this figure legend, the reader is referred to the web version of this article.)

(ii) for $C_Y \geq 10^{-2}$, the displacement $-z/L$ suddenly increases. This sharp increase at $C_Y \approx 10^{-2}$ is due to the kirigami sheet undergoing buckling that can be highlighted in our FIRM model by plotting the profile of the sheet's midplane in Fig. 4b, i.e., at $x = W/2$, for increasing Cauchy numbers. We note that this profile deforms symmetrically for low Cauchy numbers, but that at $C_Y \approx 10^{-2}$ the deformation becomes asymmetric. We quantify the predicted asymmetry in Fig. 4c by plotting the maximum vertical displacement z/L and its corresponding lateral x/L displacement for each Cauchy number (yellow dash–dot line). Again, our prediction agrees with the experimental data from Marzin et al. [14] (see markers in Fig. 4c).

3.4. Flow-induced draping of a disk

Finally, we test the limits of our FIRM software by studying a circular flexible plate draping, i.e., reconfiguring, under a uniform flow normal to its initial surface (see Fig. 5a). This problem is degenerate as multiple solutions can be found for the same applied load. Schouveiler and Eloy [22] studied experimentally the shape transition of flow-induced draping of a circular plate and observed four different modes of deformation governed by the Cauchy number: (i) a cylindrical mode (mode C), a (ii) two-fold (mode $2F$), and (iii) three-fold ($3F$) conical modes and (iv) a bent three-fold mode (mode $3F^*$). Capturing the transitions between each deformation mode is numerically challenging due to the coexistence of many solutions. Energetic approaches to identify the prevalent mode, as discussed by Schouveiler and Eloy [22], or numerical damping added to the Newton and Arc Length solvers implemented in the FIRM model could be incorporated, but this is out of the scope of this work. Here, to simplify computations while retaining the physics of the flow-induced reconfiguration, we capture various N-fold symmetric deformation modes by modeling a $1/(2N)$ sector of a circular plate of radius $R_e = 70\,\text{mm}$, clamped at its center of radius $R_i = 6\,\text{mm}$, and of thickness $T = 75\,\mu\text{m}$ using symmetry planes on its sides. The plate's material is modeled using a Young's modulus $E = 3\,\text{GPa}$ and Poisson's ratio $\nu = 0.3$, with the flow modeled using a density $\rho_f = 1.225\,\text{kg}\,\text{m}^{-3}$, the rigid drag coefficient $C_D = 2.0$, and velocity U_∞. For this case, the Cauchy number is obtained from Eq. (4) by setting $L_c = R_e$ and $K = ET^3 \ln\left(R_e/R_i\right) / \left(12(1-\nu^2)R_e^2\right)$ [22].

When we set $N = \{2, 3, 4, 5, 6\}$, we obtain the corresponding deformation modes C, $3F$, $4F$, $5F$ and $6F$ shown in Fig. 5b, and mode $0F$ is obtained during all simulations for sufficiently low Cauchy numbers, as it is a stretching mode that is purely axisymmetric. In Fig. 5b, the colormap represents the angle the disks make with the flow, but are taken at arbitrary Cauchy numbers, such that their exact value is

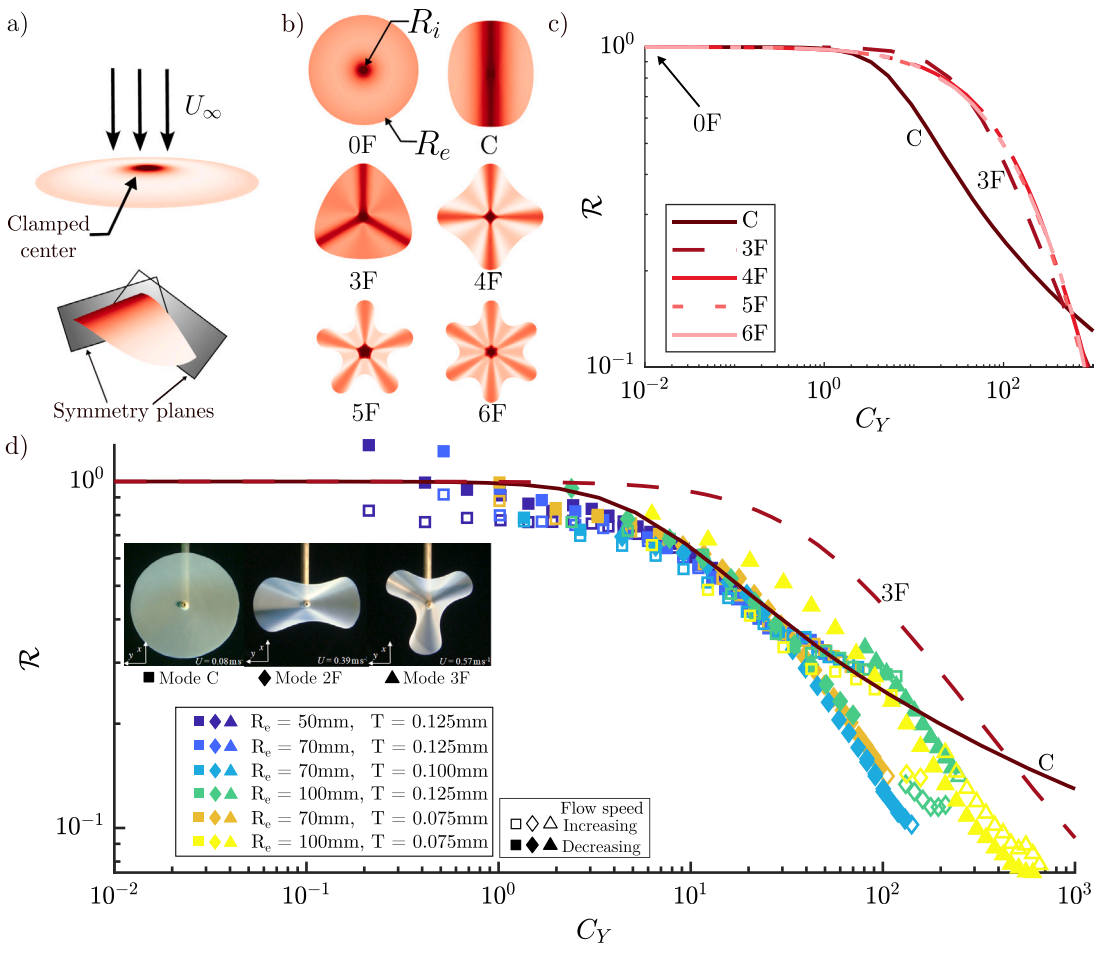

Fig. 5. Draping of a circular plate under flow. (a) Schematic of the disk under flow and its simplification through symmetry planes. (b) Predicted deformation modes of a circular plate under flow. Mode $0F$ shows the external radius R_e and clamped radius R_i of the plate. (c) Reconfiguration number $\mathcal{R}$ as a function of the Cauchy number C_Y for the different deformation modes of the circular plate. (d) Reconfiguration number $\mathcal{R}$ as a function of the Cauchy number C_Y of modes C and $3F$ compared with wind tunnel measurements. Snapshots of the experimental deformations adapted from Schouveiler and Eloy [22] are added in the insets with permission (https://doi.org/10.1103/PhysRevLett.111.064301). (For interpretation of the references to color in this figure legend, the reader is referred to the web version of this article.)

not qualitatively important, but the colormap is used to illustrate the deformation modes. Note that when we set $N = 2$, we force mode C to appear, without being able to simulate mode $2F$ which coexists with mode C as they are both two-fold symmetric. We are also unable to simulate mode $3F^*$ as it has only one symmetry plane and would require both contacts and shading to be implemented.

In Fig. 5c, we show the $\mathcal{R}$-C_Y curves of the simulated axisymmetric deformation modes. At low Cauchy numbers, i.e., $C_Y < 1$, we find that the circular plate behaves similarly to its rigid counterpart, regardless of the imposed mode of deformation. As we increase the Cauchy number, the reconfiguration number decreases at different rates depending on the mode of reconfiguration. Below $C_Y \approx 500$, mode C shows the smallest reconfiguration number, until modes $3F$ to $6F$ sequentially reach smaller reconfiguration numbers.

Finally, in Fig. 5d, we plot wind tunnel data of flow-induced draping of circular plates with varying geometry (see [31] for details regarding our wind tunnel experiments), both when increasing (empty symbols) and decreasing (solid symbols) the flow velocity, exhibiting deformation hysteresis. The square, diamond, and triangular markers identify the mode of deformation C, $2F$, and $3F$, respectively. We overlay in Fig. 5d the $\mathcal{R}$-C_Y curves predicted by FIRM for modes C and $3F$. We find excellent agreement with the experimental data when deforming in mode C. However, for increasing flow speed (empty symbols), as mode C transitions to mode $2F$ at $C_Y \approx 100$ and further transitions to mode $3F$ at $C_Y \approx 200$, there is a discrepancy between the experimental results and the numerical simulations, as the C-mode simulation curve only crosses the $3F$-mode curve at $C_Y \approx 400$. This discrepancy can be due to flow physics unaccounted for by our simplified flow model, such as irregular wake phenomena, but also to the coexistence of different possible solutions. Nevertheless, we observe that the numerical and experimental curves still follow a similar trend, they are only shifted in Cauchy.

4. Conclusion and outlook

In conclusion, the developed FIRM framework captures complex nonlinearities observed in coupled fluid–structure interaction problems without the use of CFD while maintaining high generality and simple setup requirements. Where previous studies focused on specific theories for singular geometries or on coupled CFD-FEA software, here, we build upon a corotational finite element formulation by developing a simpler formulation of the pressure drag associated with the flow. We compare the results obtained from using this new numerical implementation with different theoretical, numerical, and experimental results obtained from the literature [3,4,14,22,23] as well as experiments performed in a wind tunnel on draping disks. Even though we do not model shading and contact physics, we find excellent agreement with many previously developed models. Indeed, while a simplified shading model was implemented for the reconfigured disk with a cut, no generalized shading laws are currently implemented. Moreover, it is possible to implement simpler formulations for non-modeled physics within the solver for specific cases, as was performed for the disk with radial slits

and the kirigami sheet under flow. Due to the custom nature of the framework, it is also possible to add other physics on top of the flow-induced pressure field, such as skin friction [39], buoyancy [11,40,41], pressurized membranes [42], magnetic loads [43], etc., and therefore solve a large array of highly coupled and nonlinear problems. For example, snapping mechanisms, such as those used for flow control [13, 44] or those observed in origami structures [15], could be studied under flow using this framework. Moreover, it is also possible to add more complex material laws into the software to model hyperelastic, viscoelastic and plastic materials.

CRediT authorship contribution statement

Danick Lamoureux: Writing – review & editing, Writing – original draft, Visualization, Validation, Software, Methodology, Investigation, Funding acquisition, Formal analysis, Data curation, Conceptualization. **Sophie Ramananarivo:** Writing – review & editing, Supervision, Project administration, Methodology, Investigation, Formal analysis, Conceptualization. **David Melancon:** Writing – review & editing, Supervision, Resources, Project administration, Investigation, Funding acquisition, Formal analysis, Conceptualization. **Frédérick P. Gosselin:** Writing – review & editing, Supervision, Resources, Project administration, Methodology, Investigation, Funding acquisition, Formal analysis, Conceptualization.

Declaration of competing interest

The authors declare the following financial interests/personal relationships which may be considered as potential competing interests: Frederick Gosselin reports financial support was provided by Natural Sciences and Engineering Research Council of Canada. Danick Lamoureux reports financial support was provided by Natural Sciences and Engineering Research Council of Canada. Danick Lamoureux reports financial support was provided by Quebec Research Fund Nature and Technology. David Melancon reports financial support was provided by Natural Sciences and Engineering Research Council of Canada. If there are other authors, they declare that they have no known competing financial interests or personal relationships that could have appeared to influence the work reported in this paper.

Acknowledgments

The financial support of the Natural Sciences and Engineering Research Council of Canada (Funding Reference No. RGPIN-2019-7072) is acknowledged. D.L. acknowledges funding by a NSERC BESC-M scholarship, the NSERC's Supplément pour Études à l'Étranger BESC-SEEMS, and a Fonds de Recherche du Québec - Nature et Technologies's (FRQNT) master scholarship. S.R acknowledges support from a JCJC Agence Nationale de la Recherche grant (ANR-20-CE30-0009-01).

Appendix A. Supplementary data

Supplementary material related to this article can be found online at https://doi.org/10.1016/j.eml.2024.102271.

Data availability

A Github repository has been made public to share the code and data.

References

[1] P. Lin, G. Hu, K. Tse, J. Song, A.K. Leung, Z. Jiang, L. Zou, Characterizing wind-induced reconfiguration of coaxial branched tree, Agricult. Forest. Meterol. (2023) http://dx.doi.org/10.1016/j.agrformet.2023.109590.
[2] S. Alben, M. Shelley, J. Zhang, Drag reduction through self-similar bending of a flexible body, Nature (2002) http://dx.doi.org/10.1038/nature01232.
[3] L. Schouveiler, A. Boudaoud, The rolling up of sheets in a steady flow, J. Fluid Mech. (2006) http://dx.doi.org/10.1017/S0022112006000851.
[4] F. Gosselin, E. de Langre, B.A. Machado-Almeida, Drag reduction of flexible plates by reconfiguration, J. Fluid Mech. (2010) http://dx.doi.org/10.1017/S0022112009993673.
[5] E. De Langre, A. Gutierrez, J. Cossé, On the scaling of drag reduction by reconfiguration in plants, C. R. Méc. (2012) http://dx.doi.org/10.1016/j.crme.2011.11.005.
[6] F.P. Gosselin, Mechanics of a plant in fluid flow, J. Exp. Bot. (2019) http://dx.doi.org/10.1093/jxb/erz288.
[7] S.A. Etnier, S. Vogel, Reorientation of daffodil(*Narcissus* : Amaryllidaceae) flowers inwind: drag reduction andtorsional flexibility, Am. J. Bot. 87 (1) (2000) 29–32.
[8] B.-H. Sun, X.-L. Guo, Drag scaling law and parachute terminal velocity of the dandelion, AIP Adv. (2023) http://dx.doi.org/10.1063/5.0155103.
[9] Y. Luna Lin, M. Pezzulla, P.M. Reis, Fluid–structure interactions of bristled wings: the trade-off between weight and drag, J. R. Soc. Interface 20 (206) (2023) 20230266, https://royalsocietypublishing.org/doi/abs/10.1098/rsif.2023.0266.
[10] P.T. Martone, M. Boller, I. Burgert, J. Dumais, J. Edwards, K. Mach, N. Rowe, M. Rueggeberg, R. Seidel, T. Speck, Mechanics without Muscle: Biomechanical inspiration from the plant world, Integr. Comp. Biol. 50 (2010) http://dx.doi.org/10.1093/icb/icq122.
[11] X. Zhang, H. Nepf, Flow-induced reconfiguration of aquatic plants, including the impact of leaf sheltering, Limnol. Oceanogr. 65 (11) (2020) http://dx.doi.org/10.1002/lno.11542.
[12] S. Vogel, Drag and flexibility in sessile organisms, Amer. Zool. 24 (1) (1984) 37–44.
[13] M. Gomez, D.E. Moulton, D. Vella, Passive control of viscous flow via elastic snap-through, Phys. Rev. Lett. (2017) http://dx.doi.org/10.1103/PhysRevLett.119.144502.
[14] T. Marzin, K. Le Hay, E. de Langre, S. Ramananarivo, Flow-induced deformation of kirigami sheets, Phys. Rev. Fluids (2022) http://dx.doi.org/10.1103/PhysRevFluids.7.023906.
[15] T. Marzin, E. de Langre, S. Ramananarivo, Shape reconfiguration through origami folding sets an upper limit on drag, Proc. R. Soc. Lond. Ser. A Math. Phys. Eng. Sci. 478 (2022).
[16] A.K. Pandey, G. Sharma, R. Bhardwaj, Flow-induced reconfiguration and cross-flow vibrations of an elastic plate and implications to energy harvesting, J. Fluids Struct. 122 (2023) 103977.
[17] Z. Wang, F. Zhao, Y. Fu, F. Deng, L. Zeng, J. Cui, Towards energy harvesting through flow-induced snap-through oscillations, Int. J. Mech. Sci. 254 (2023) 108428.
[18] M. Song, J. Yoo, J. Ham, D. Kim, Three-dimensional reconfiguration of an elastic sheet with unidirectional side flaps, J. Fluid Mech. (2022) http://dx.doi.org/10.1017/jfm.2022.970.
[19] M. Guttag, H.H. Karimi, C. Falcón, P.M. Reis, Aeroelastic deformation of a perforated strip, Phys. Rev. Fluids (2018) http://dx.doi.org/10.1103/PhysRevFluids.3.014003.
[20] M. Pezzulla, E.F. Strong, F. Gallaire, P.M. Reis, Deformation of porous flexible strip in low and moderate Reynolds number flows, Phys. Rev. Fluids 5 (8) (2020) 084103.
[21] M. Boukor, A. Choimet, É. Laurendeau, F.P. Gosselin, Flutter limitation of drag reduction by elastic reconfiguration, Phys. Fluids 36 (2) (2024) 021915, https://pubs.aip.org/aip/pof/article-pdf/doi/10.1063/5.0193649/19702290/021915_1_5.0193649.pdf.
[22] L. Schouveiler, C. Eloy, Flow-induced draping, Phys. Rev. Lett. (2013) http://dx.doi.org/10.1103/PhysRevLett.111.064301.
[23] R.-N. Hua, L. Zhu, X.-Y. Lu, Dynamics of fluid flow over a circular flexible plate, J. Fluid Mech. (2014) http://dx.doi.org/10.1017/jfm.2014.571.
[24] M.C. Vanzulli, J.M. Pérez Zerpa, A co-rotational formulation for quasi-steady aerodynamic nonlinear analysis of frame structures, Heliyon 9 (9) (2023) e19990.
[25] J. Lee, I. Seo, S. Lee, Propulsion velocity of a flapping wing at low Reynolds number, J. Fluids Struct. 54 (2015) 422–439.
[26] J. Lee, S. Lee, The flexibility effect of a plate according to various angles of attack in a free-stream, J. Fluids Struct. 51 (2014) 40–54.
[27] G. Taylor, Analysis of the swimming of long and narrow animals, Proc. R. Soc. A 214 (1117) (1952) 158–183.
[28] A. Bhati, R. Sawanni, K. Kulkarni, R. Bhardwaj, Role of skin friction drag during flow-induced reconfiguration of a flexible thin plate, J. Fluids Struct. 77 (2018) 134–150.
[29] F. Caselli, P. Bisegna, Polar decomposition based corotational framework for triangular shell elements with distributed loads: Corotational framework with distributed loads, Internat. J. Numer. Methods Engrg. (2013) http://dx.doi.org/10.1002/nme.4528.

[30] C. Geuzaine, J.-F. Remacle, Gmsh: a three-dimensional finite element mesh generator with built-in pre- and post-processing facilities, Internat. J. Numer. Methods Engrg. 79 (2009).
[31] D. Lamoureux, S. Ramananarivo, D. Melancon, F.P. Gosselin, Supplementary information, 2024.
[32] J.-L. Batoz, K.-J. Bathe, L.-W. Ho, A study of three-node triangular plate bending elements, Internat. J. Numer. Methods Engrg. (1980) http://dx.doi.org/10.1002/nme.1620151205.
[33] C. Jeyachandrabose, J. Kirkhope, C.R. Babu, An alternative explicit formulation for the DKT plate-bending element, Internat. J. Numer. Methods Engrg. (1985) http://dx.doi.org/10.1002/nme.1620210709.
[34] C.A. Felippa, A study of optimal membrane triangles with drilling freedoms, Comput. Methods Appl. Mech. Engrg. (2003) http://dx.doi.org/10.1016/S0045-7825(03)00253-6.
[35] D. Lamoureux, S. Ramananarivo, D. Melancon, F.P. Gosselin, Flow-induced reconfiguration model based on the corotational finite element method (FIRM) v1.0, 2024, http://dx.doi.org/10.5281/zenodo.14225396.
[36] S. Alben, M. Shelley, J. Zhang, How flexibility induces streamlining in a two-dimensional flow, Phys. Fluids (2004) http://dx.doi.org/10.1063/1.1668671.
[37] M. Isobe, K. Okumura, Initial rigid response and softening transition of highly stretchable kirigami sheet materials, Sci. Rep. (2016) http://dx.doi.org/10.1038/srep24758.
[38] M. Isobe, K. Okumura, Continuity and discontinuity of kirigami's high-extensibility transition: A statistical-physics viewpoint, Phys. Rev. Res. (2019) http://dx.doi.org/10.1103/PhysRevResearch.1.022001.
[39] A. Bhati, R. Sawanni, K. Kulkarni, R. Bhardwaj, Role of skin friction drag during flow-induced reconfiguration of a flexible thin plate, J. Fluids Struct. (2018) http://dx.doi.org/10.1016/j.jfluidstructs.2017.12.003.
[40] M. Luhar, H.M. Nepf, Flow-induced reconfiguration of buoyant and flexible aquatic vegetation, Limnol. Oceanogr. 56 (6) (2011) 2003–2017.
[41] T.I. Marjoribanks, M. Paul, Modelling flow-induced reconfiguration of variable rigidity aquatic vegetation, J. Hydraul. Res. 60 (1) (2022) 46–61.
[42] Z. Chen, C. Wei, Z. Li, C. Zeng, J. Zhao, N. Hong, N. Su, Wind-induced response characteristics and equivalent static wind-resistant design method of spherical inflatable membrane structures, Buildings 12 (10) (2022) http://dx.doi.org/10.3390/buildings12101611.
[43] A. Abbasi, T.G. Sano, D. Yan, P.M. Reis, Snap buckling of bistable beams under combined mechanical and magnetic loading, Phil. Trans. R. Soc. A 381 (2244) (2023) 20220029.
[44] H. Kim, M. Lahooti, J. Kim, D. Kim, Flow-induced periodic snap-through dynamics, J. Fluid Mech. 913 (2021) A52.